Fine Thermal Control Based on Multilayer Temperature Distribution for Lithium-Ion Batteries

Zhechen Guo, Jun Xu, *Senior Member, IEEE*, Xingzao Wang, Jinwen Shi, Enhu Li, and Xuesong Mei

***Abstract*—To achieve fine control of multilayer temperature uniformity and energy consumption in a battery thermal management system (BTMS), a model predictive control (MPC) based on the reduced-order model and the heat generation previewer is proposed in this work. A direct contact liquid cooling battery pack is adopted to verify the control strategy. The control-oriented reduced-order model is developed for online multilayer temperature distribution acquisition. A heat generation predictor coupling with a dual neural network is integrated into the MPC controller to provide accurate future disturbances preview. The results indicate that the BTMS can be controlled to the target temperature with less overshoot. Besides, the temperature difference of the cell, module, and pack level can be limited to 0.8 °C, 1 °C, and 2 °C, respectively, decreasing the state of health difference among the cells. For energy consumption, the proposed method improves up to 56.48%.**

***Index Terms*—Battery thermal management, energy consumption, model predict control, reduced-order model, temperature uniformity.**

I. Introduction

THE rapid popularization of electric vehicles (EVs) has aroused great attention to safety issues [1]. Lithium-ion batteries (LIBs) are vulnerable to temperature that an excessively high or low temperature will be detrimental to their safety, durability, efficiency, etc. [2]. The thermal performance of LIBs is generally regulated by battery thermal management system (BTMS) in EVs with large battery packs. The main objective of BTMS is to control the batteries within the optimal temperature range, normally from 20“°C to 40“°C [3], [4]. Besides, it is important to address temperature uniformity since it has a significant impact on the consistency of the batteries, which in turn impacts their capacity, longevity, and other properties [5], [6]. Therefore, a significant development trend is toward fine thermal management, where both the temperature range and the temperature difference should be well controlled. However, achieving fine control of BTMS remains challenging due to the lack of real-time information on the multilayer temperature distribution [7], [8].

In practice, BTMSs are generally combined with the passenger cabin heating-ventilation-air-conditioning (HAVC) system or other heat dissipation components, such as the heat pump air condition system integrated in Tesla [9]. Compared with traditional fossil fuels, LIBs have lower energy density with a longer time to full charge, which causes “range anxiety.” The thermal management component is one of the main energy-consuming sources in EVs, such as refrigeration and heating equipment [10]. The relevant energy consumption is particularly obvious in the battery packs with large capacity. Researches have shown that the driving range can be reduced by 40% when the HAVC systems are utilized [11]. When facing extreme weather, the large additional power consumption is inevitable [12], [13]. Therefore, the control strategy of the BTMS should be comprehensive optimized in terms of thermal performance, energy consumption, and even for the life span [14], [15].

The integrated control strategy at present, such as the rule-based control [16], proportion integration differentiation control [17], and fuzzy control [18], are feasible to limit the temperature within the optimum range according to the real-time feedback through the temperature sensors. Further, some active control methods have been adopted to adjust the maximum temperature and temperature uniformity in the air cooling-based BTMS [19]. Nevertheless, although such methods are robust and easy to implement, the control delay is readily apparent. The large inertia of thermal systems results in a lagged response of control outputs and variables, leading to significant overshoot and energy loss. To solve such problems, some optimal control methods have been introduced in BTMS. By combining with the *priori* information, both the system response and energy efficiency

Manuscript received 16 May 2023; revised 12 August 2023; accepted 21 September 2023. Date of publication 10 October 2023; date of current version 23 February 2024. This work was supported in part by the National Natural Science Foundation of China under Grant 52075420, and in part by the National Key Research and Development Program of China under Grant 2020YFB1708400. Paper no. TII-23-1742. *(Corresponding author: Jun Xu.)*

Zhechen Guo, Jun Xu, Xingzao Wang, and Xuesong Mei are with the State Key Laboratory for Manufacturing Systems Engineering, Xi'an Jiaotong University, Xi'an 710049, China, and also with the Shaanxi Key Laboratory of Intelligent Robots, Xi'an Jiaotong University, Xi'an 710049, China (e-mail: gzc1618@stu.xjtu.edu.cn; xujunx@mail.xjtu.edu.cn; 3045740851@qq.com; xsmei@xjtu.edu.cn).

Jinwen Shi is with the State Key Laboratory of Multiphase Flow in Power Engineering, Xi'an Jiaotong University, Xi'an 710049, China (e-mail: jinwen_shi@mail.xjtu.edu.cn).

Enhu Li is with the Gresgying Digital Energy Technology Company, Ltd., Xianyang 276022, China (e-mail: leh@gresgying.com).

Color versions of one or more figures in this article are available at https://doi.org/10.1109/TII.2023.3320358.

Digital Object Identifier 10.1109/TII.2023.3320358

are taken into account. Lee et al. [20] applied Pontryagin's maximum principle in controlling temperature and energy. The dynamic programming (DP) algorithm has been introduced in the optimal control trajectory to achieve global cost optimization [21]. Besides, machine learning methods have been developed to improve the control effect. However, the insufficient *priori* information and calculation complexity hinder the online application of these methods.

The model predictive control (MPC) method is an attractive solution due to its fast response times and real-time optimization capabilities. Meanwhile, it has less computational complexity compared with the DP method. The control variables can be changed in advance to prevent an overshoot in the high inertia system by predicting the temperature trend. The MPC-based schemes have been conducted in BTMSs by some researchers. Xie et al. [22] considered the battery life in the MPC-based battery temperature control. Zhuang et al. [23] adopted fuzzy MPC to adjust the cooling efficiency of an air-cooling-based BTMS. A stochastic model with unequally spaced probability distribution was adopted in MPC control according to the work in [24], the results show the improvements of thermal performance and less energy consumption. Zhao et al. proposed a two-layer MPC strategy for BTMS and HVAC coupled system to improve the real-time implementation capability [25], [26]. Similarly, a hierarchical MPC was utilized in connected and autonomous vehicles to reduce energy cost in [27]. In an air-based BTMS, Liu et al. [28] and [29] explored the MPC controller in combination with the variable structure to obtain good control effectiveness. The cooling channel could be switched to different types to adapt to different situations.

As mentioned earlier, thermal uniformity plays a crucial role in determining the capacity and lifespan of a battery system. However, the multilayer temperature distribution has seldom been considered in the above-mentioned MPC-based methods used in BTMS, making it difficult to achieve fine temperature control. The single cell is considered as a homogeneous body with uniform temperature distribution in most existing researches. Actually, a substantial temperature differential within a single cell is not uncommon, which is measurable in the high-rate charge/discharge process [30]. Besides, the temperature differences for a battery pack are not easy to be obtained online, making fine temperature control difficult. Additionally, the accuracy of the model directly impacts the effectiveness of control, resuting the uncertainty in forecasting. It accordingly hinders the online optimization for the MPC.

To address these issues, a reduced-order multiphysics coupling model is proposed in this work to depict the multilayer temperature distribution online. Besides, a composite neural network (NN) model is put forward to predict future heat generation. The fine thermal control for BTMS is achieved through the MPC method by integrating the temperature distribution model and heat generation predictor. The MPC algorithm is applied in a direct-contact liquid cooling system (DCLCS) with four control inputs. The proposed method is verified experimentally and compared with the traditional rule-based control strategy to demonstrate its superiority in thermal performance and energy saving. Furthermore, the state of health difference (dSOH) among the cells caused by temperature inconsistency is also studied. The main contribution of this work is designing a novel thermal control system that achieve fine control of multilevel temperature for battery packs. The online prediction of multilayer temperature is the prominent innovation that achieved by the multiphysics reduced-order model and dual NN-based predictor. The MPC strategy is conducted on this basis. The proposed methods make efforts to explore the optimal BTMS design and control.

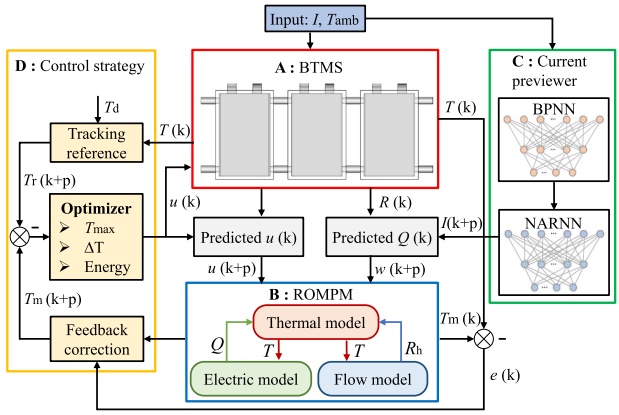

Fig. 1. Framework of the proposed MPC-based BTMS control strategy.

The rest of this article is organized as follows. Section II introduces the MPC-based control method. The experiment platform is described in Section III. In Section IV, the control effect of the proposed scheme is validated and compared with other strategies. Section V presents the main conclusions.

II. MPC-Based BTMS Control Strategy

The proposed framework of the MPC-based BTMS control strategy is presented in Fig. 1. The proposed control strategy mainly includes four parts: 1) the DCLCS; 2) the control-oriented predictive model; 3) the heat generation predictor integrating with the dual NN-based current previewer; 4) the MPC part, which including the feedback correction, reference trajectory, and receding horizontal optimizer. The reduced-order multifield coupled model comprises the electrical, thermal, and flow submodels. The specific contents will be introduced in the following sections.

A. Control System Design of the Liquid-Based BTMS

In this work, the proposed control strategy is applied in a battery pack integrated with DCLCS. To concisely explain the method, the battery pack consists of three modules, each with six interconnected battery cells. The temperature uniformity includes threefold: cell, module, and pack. The uneven temperature of the single cell is mainly attributed to the effectiveness of the tabs [31]. At the module level, the temperature uniformity is determined by the coolant flow, where the coolant temperature becomes the dominant factor at the pack level.

To achieve the fine control of multilayer thermal performance, the control system of the liquid-based BTMS is designed as

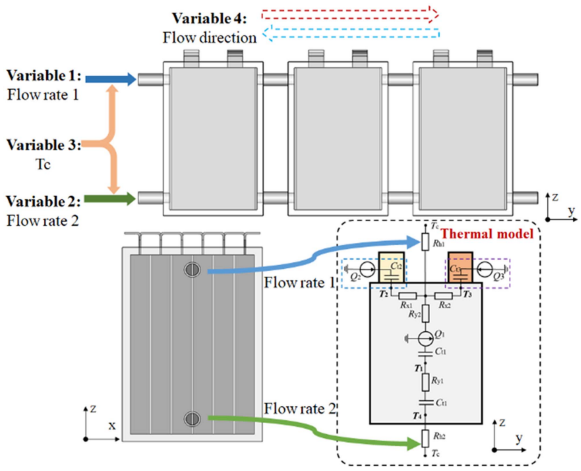

Fig. 2. Direct-contact liquid cooling BTMS and the control design.

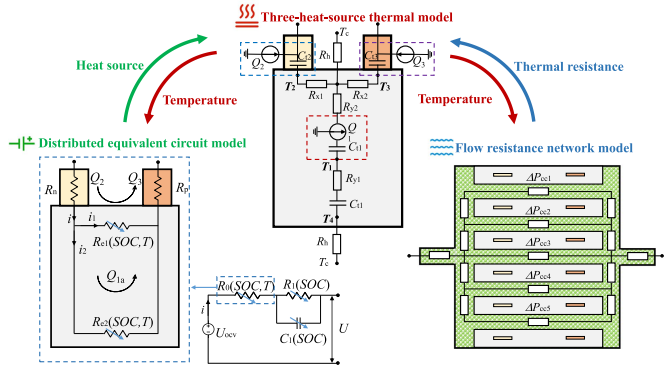

Fig. 3. Reduced-order multiphysics coupling model for liquid-cooling BTMS.

shown in Fig. 2. Four control variables are applied to adjust the thermal performance of different levels, namely the flow rate 1–2, T_c, and the flow direction. The coolant flows through two pathways responding to the upper and lower sides to reduce the temperature difference in the cell level. The total flow rate is determined by the pump, where the flow distribution is determined by the solenoid valve. To meet the heat exchange requirements, the coolant temperature control is critical, which is also the main source of the energy consumption. To restrain the uneven temperature distribution of different modules caused by the coolant temperature variation, the reciprocation flow is available that determined by the pump. As a whole, fine thermal control can be achieved by combining the above-mentioned four control inputs.

B. Control-Oriented Reduced-Order Model

In this work, a DCLCS is employed as a case study for analysis purposes. The battery pack is composed of three battery modules with the same structure. To describe the multilayer temperature distribution in real time with less computation cost, a reduced-order multiphysics coupling model is established consisting of three main submodels: the electrical model, the thermal model, and the flow model. The electrical model is applied to describe the heat generation mechanism of the battery, and the flow model is adopted to calculate the difference in heat dissipation characteristics among the cells. The schematic diagram of the submodels and their relationship is shown in Fig. 3.

1) Electrical Model: The electrical model is derived from the Thevenin equivalent model that involves the state of charge (SOC), terminal voltage, open-circuit voltage, distributed resistance, and capacitance. The heat generation rate of different heat sources is calculated by the electrical model and sent to the thermal model to characterize the uneven heat production of the single cell. The relevant equations are expressed as follows:

$$\begin{aligned} R_0 &= R_\mathrm{p} + R_\mathrm{n} + \frac{R_{e1}R_{e2}}{R_{e1}+R_{e2}} \\ U &= U_{ocv} + iR_0 + U_1 \\ \frac{dU_1}{dt} &= -\frac{U_1}{R_1C_1} + \frac{i}{C_1} \end{aligned} \tag{1}$$

where R_p and R_n represent the internal resistance of the positive and negative tabs, which is determined by the material of current collectors.

2) Thermal Model: The three-heat-source thermal model is proposed to calculate the nonuniform temperature distribution of the single cell. The heat production rate of the three independent heat sources (Q_1, Q_2, and Q_3) can be calculated according to the distributed resistance, formulated as follows:

$$\begin{aligned} Q_1 &= i_2^2R_{e2} + \frac{U_1^2}{R_1} + i_2T_1\frac{\partial U}{\partial T_1} \\ Q_2 &= i^2R_\mathrm{n} + \frac{i_1^2R_{e1}}{2} \\ Q_3 &= i^2R_\mathrm{p} + \frac{i_1^2R_{e1}}{2} \end{aligned} \tag{2}$$

On this basis, the uneven temperature can be presented by four feature points (T_1, T_2, T_3, and T_4), which are arranged nearby the two tabs, center and bottom of the cell, respectively. The temperature of four feature points is derived as follows:

$$\begin{aligned} C_\mathrm{t}\frac{dT_2}{dt} &= Q_2 - \frac{T_2-T_\mathrm{c}}{R_\mathrm{h}+R_\mathrm{x1}} - \frac{T_2-T_1}{R_{y2}+R_{x1}} - \frac{T_2-T_3}{R_{x1}+R_{x2}} - \frac{T_2-T_{amb}}{R_{air}} \\ C_\mathrm{t}\frac{dT_3}{dt} &= Q_3 - \frac{T_3-T_\mathrm{c}}{R_\mathrm{h}+R_\mathrm{x2}} - \frac{T_3-T_1}{R_{y2}+R_{x2}} - \frac{T_3-T_2}{R_{x1}+R_{x2}} - \frac{T_3-T_{amb}}{R_{air}} \\ C_\mathrm{t}\frac{dT_1}{dt} &= Q_1 - \frac{T_1-T_4}{R_{y1}} + \frac{T_2-T_1}{R_{y2}+R_{x1}} + \frac{T_3-T_1}{R_{y2}+R_{x2}} \\ C_\mathrm{t}\frac{dT_4}{dt} &= \frac{T_1-T_4}{R_{y1}} - \frac{T_4-T_\mathrm{c}}{R_\mathrm{h}} \end{aligned} \tag{3}$$

where C_t represents the equivalent thermal capacity of battery. R_x1, R_x2, R_y1, and R_y2 are the equivalent thermal resistances that require accurate identification. R_h represents the thermal resistance that indicates the effect of convective heat transfer between the cell and coolant.

3) Flow Model: The temperature inhomogeneity of different cells in the module is mainly caused by various heat dissipation conditions. The cooling efficiency mainly depends on two aspects: the temperature difference and convection heat transfer intensity, where the latter factor is positively correlated with the flow velocity. The flow resistance network model (FRNM) is applied to fast calculate the velocity distribution. The expressions of the FRNM can be written as follows:

$$\Delta P_{\mathrm{loss},FC2,\mathrm{i}} + \Delta P_{\mathrm{loss},MC2,\mathrm{i}} + \Delta P_{\mathrm{loss},RC2,\mathrm{i}} - \Delta P_{\mathrm{loss},MC3,\mathrm{i}} = 0 \tag{4}$$

$$\Delta P_\mathrm{loss} = \Delta P_\mathrm{local} + \Delta P_\mathrm{friction} \tag{5}$$

where ΔP_{loss} represents the total pressure loss, containing the local pressure loss ΔP_{local} and friction pressure loss $\Delta P_{\text{friction}}$. *FC*, *MC*, and *RC* stand for the front channel, middle channel, and rear channel, respectively. The local pressure loss and friction pressure loss can be expressed by the function of coolant velocity, as follows [32]:

$$\begin{aligned}
\Delta P_{\text{friction,FC2,i}} &= \lambda_{\text{FC2,i}} \frac{l_{\text{DP2,i}}}{2D_{\text{DP2,i}}} \rho v_{\text{FC2,i}}^2 \\
\Delta P_{\text{friction,RC2,i}} &= \lambda_{\text{RC2,i}} \frac{l_{\text{CP2,i}}}{2D_{\text{CP2,i}}} \rho v_{\text{RC2,i}}^2 \\
\Delta P_{\text{friction,MC2,i}} &= \lambda_{\text{MC2,i}} \frac{l_{\text{MC2,i}}}{2D_{\text{MC2,i}}} \rho v_{\text{MC2,i}}^2
\end{aligned} \tag{6}$$

$$\begin{aligned}
\Delta P_{\text{local,FC2,i}} &= \frac{\xi_{\text{FC2,i}}}{2} \rho v_{\text{FC2,i}}^2 \\
\Delta P_{\text{local,RC2,i}} &= \frac{\xi_{\text{RC2,i}}}{2} \rho v_{\text{RC2,i}}^2 \\
\Delta P_{\text{local,MC2,i}} &= \frac{\xi_{\text{FC}\to\text{MC2,i}}}{2} \rho v_{\text{FC2,i}}^2 + \frac{\xi_{\text{MC}\to\text{RC2,i}}}{2} \rho v_{\text{RC2,i}}^2
\end{aligned} \tag{7}$$

where v represents the equivalent flow velocity of each flow channel, ρ represents the coolant density, l and D are the length and the equivalent diameter of each channel. ξ and λ represent the dimensionless friction constant and local differential pressure coefficient. In addition, according to the mass conversation law, the following equations can be deduced from the inlet/outlet node:

$$\begin{aligned}
V_{\text{c}} &= v_{\text{PP,i}} A_{\text{PP,i}} \\
v_{\text{PP,i-1}} A_{\text{PP1,i-1}} &= v_{\text{MC3,i}} A_{\text{MC3,i}} + 2 v_{\text{FC2,i}} A_{\text{FC2,i}} \\
v_{\text{PP2,i}} A_{\text{PP2,i}} &= v_{\text{MC3,i}} A_{\text{MC3,i}} + 2 v_{\text{RC2,i}} A_{\text{RC2,i}}
\end{aligned} \tag{8}$$

where A represents the cross-sectional area of each channel. The coolant velocity of each channel can be calculated by solving the above-mentioned series of equations. Thereby, R_{h} can be obtained according to the relationship as follows:

$$R_{h,i} = Y_m v_{MC,i}^{-y} \tag{9}$$

where Y_{m} and y are the corresponding coefficient that derived from the parameter identification or empirical formula.

By coupling with the three reduced-order submodels, the temperature distribution of the cell, module, and pack level can be calculated with less computation burden, which provides an excellent basement for multilayer temperature uniformity control. The temperature distribution of the three level can be calculated within ten milliseconds in the prediction horizon through the control-oriented model, so the rolling optimization can be achieved in real time.

C. Battery Heat Generation Prediction

To obtain the temperature trend in the prediction horizon, the heat generation preview is necessary. The heat production rate of the battery is mainly determined by the current and internal resistance, where the resistance is relatively stable in short time intervals. Consequently, the problem is transformed to the prediction of the future current. Since the speed prediction based on NN has been widely applied with insufficient generalization ability, the historical current data is used to predict the future current analogically [33]. To make up for defects of the insufficient generalization ability with single NN method, a dual NN based on the operating mode recognition and current prediction is proposed to improve the prediction accuracy.

The heat generation prediction framework is displayed in Fig. 4. Six typical driving cycles are utilized to train the network,

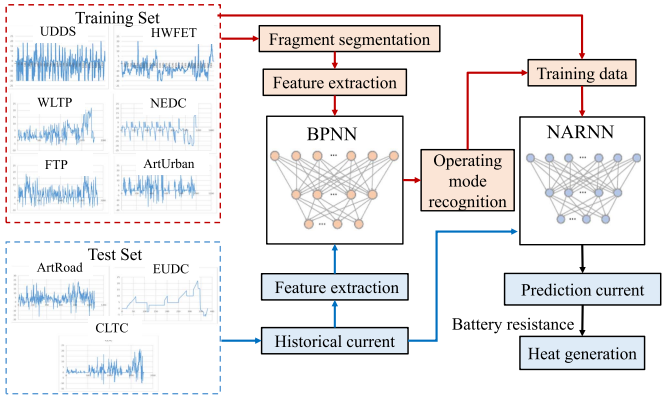

Fig. 4. Framework of heat generation prediction.

including the Urban Dynamometer Driving Schedule (UDDS), High Way Fuel Economy Test (HWFET), World Light Vehicle Test Procedure (WLTP), New European Driving Cycle (NEDC), Federal Test Procedure (FTP), and ArtUrban that containing a variety of charging/discharging scenarios. Three other driving cycles are set as test set [ArtRoad, Extra Urban Driving Cycle (EUDC), and China Light-duty vehicle Test Cycle (CLTC)] [34]. The back propagation neural network (BPNN) is used to conduct the operating mode recognition, which has the ability of arbitrarily complex pattern classification, and widely used in the field of pattern recognition. The training set is divided into lots of segments with a data length no more than 100, and the features of those segments are extracted for network training.

Twelve features are employed to identify different operating modes, including the acceleration ratio, the deceleration ratio, the constant ratio, the idle ratio, the average current, the average nonzero current, the maximum current, the average acceleration, the maximum acceleration, the minimum acceleration, the current standard deviation, and the acceleration standard deviation. The twelve features implying from the historical current are used as the input of BPNN, and the mode recognition result is the output. By determining the operating mode, the pertinent training is adopted for current prediction through the nonlinear auto-regression neural network (NARNN), which has feedback and memory functions, with significant advantages in the applications of modeling and simulating dynamic changes in time series. We have trained different NARNN models that responding to different operating conditions. When the operating mode is determined by the BPNN, the relevant NARNN is adopted to predict the current of prediction horizon. As a result, the output is the current in prediction horizon with the input of historical current in the past 10 s. Combining with the battery resistance, the responding heat generation can be calculated. The main settings of the two NNs are displayed in Tables I and II.

D. MPC strategy for liquid-based BTMS

The objective of controller is to maintain the maximum temperature and temperature difference within an optimal range with less energy consumption with small inconsistency. The MPC control strategy make efforts to coordinating the four

TABLE I
MAIN SETTINGS OF BPNN

Parameters	Setting
Input	12 characteristic
Output	Operating condition identification results
Training data	70%
Testing data	30%
Number of hidden layer neurons	10
Minimum error of training objectives	4×10^{-7}
Learning rate	0.1
Training times	1000

TABLE II
MAIN SETTINGS OF BPNN

Parameters	Setting
Input	12 characteristic
Output	Operating condition identification results
Training data	70%
Testing data	30%
Number of hidden layer neurons	10
Minimum error of training objectives	4×10^{-7}
Learning rate	0.1
Training times	1000

control inputs to achieve a satisfactory control effect. Benefiting from the multilayer temperature distribution predicted by the reduced-order model, the fine thermal control can be realized. According to the state space equations, the temperature states can be discretized. Therefore, the thermal performance in the prediction horizon p at time step k can be obtained as displayed in the following equation:

$$T(k+i) = f(T(k+i-1), u(k+i-1), d(k+i-1)) \quad (i = 1, 2, \ldots, p-1) \tag{10}$$

where $T(k)$ represents the feature temperature of the cells, $u(k)$ represents the control inputs, and $d(k)$ is the disturbance that responding to the heat generation, each item is formulated as follows:

$$\begin{aligned} T(k) &= [T_{1,1}(k), T_{1,2}(k), \ldots, T_{n,4}(k)] \\ u(k) &= [V_c(k), T_c(k), op(k), dir(k)] \\ d(k) &= [Q_m(k) | m = 1, 2, 3] \end{aligned} \tag{11}$$

where $T_{i,j}(k)$ represents the temperature of jth characteristic point in the ith battery, $V_c(k)$ represents the total volume flow rate, $op(k)$ represents the opening of solenoid valve, and $dir(k)$ is the flow direction. In addition, the control variables are limited by some constraints

$$\begin{aligned} &0L \cdot \min^{-1} \le V_c(k) \le 2L \cdot \min^{-1} \\ &15°C \le T_c(k) \le 30°C \\ &\left|\frac{dT_c(k)}{dt}\right| \le 0.1°C, \left|\frac{dV_c(k)}{dt}\right| \le 0.5L \cdot \min^{-1} \\ &0 \le op(k) \le 1 \\ &dir(k) = \pm 1 \end{aligned} \tag{12}$$

The maximum temperature $T_{\max}$ and maximum temperature difference of the battery pack $\triangle T_{\text{pack}}$ are the basic objectives. The error between the predicted value and measured data is used as the feedback correction. The optimizer is adopted to decide the control inputs in the prediction horizon by minimizing the cost function. The definition of the cost function is crucial, which contains four folds in this work: First, the maximum temperature is tracking the reference trajectory to approach the target value. Second, the temperature difference should be controlled as small as possible. Additionally, the coolant temperature should try to maintain a steady state to avoid energy consumption through refrigeration or heating. Moreover, the volume flow rate should be kept as low as possible to reduce the power loss. The cost function is written as follows:

$$\begin{aligned} J = \sum_{j=1}^{4}\sum_{i=1}^{p} \{ & w_1[T_{r,j}(k+i) - T_j(k+i)]^2 \\ & + w_2[\Delta T_{\text{pack},j}(k+i)]^2 \\ & + w_3[T_c(k+i) - T_c(k+i-1)]^2 + w_4[V_c(k+i)]^2 \} \end{aligned} \tag{13}$$

where w_1, w_2, w_3, and w_4 represent the weighting coefficient of each term, which is allocated by the importance of each objectives. The DP method is adopted to solve the nonlinear optimal control problem with constraints. The flowchart of the optimal solution is displayed in Fig. 5. When employing the DP to search the optimal control inputs in the prediction horizon, the iterative solution is conducted from back to front step by step with the cost function update, and the optimal control sequence can be obtained. To meet the requirements of online applications, each control inputs are divided into ten variables from the minimum to the maximum value according to the constraints. To improve the control timeliness, the prediction horizon is set as 10 s, where the control horizon is set as 1 s.

III. EXPERIMENT

Fig. 6 shows the integrated test platform, where the system schematic diagram is displayed in Fig. 6(a), and the actual test bench is presented in Fig. 6(b). The platform is mainly divided into the electrical loop and the liquid-cooling loop. The host computer transfer the control commands to the controller according to the strategies, and the controller gives responding instructions to individual components.

The battery pack is composed of three battery modules with same structure, and each module contains six cells that connected in series. In the circuit connections, the three modules are also connected in series. The batteries have been screened before they are assembled to the pack to ensure the consistency of their internal resistance and capacity, and the initial SOC and state of health (SOH) are 100%. Sixteen T-type thermocouples are mounted on the battery system, where two temperature sensor are arranged at the inlet and outlet, respectively, to monitor the temperature changes of the coolant, another fourteen sensors are located on the cells surface to reflect the temperature nonuniformity of the battery module and pack.

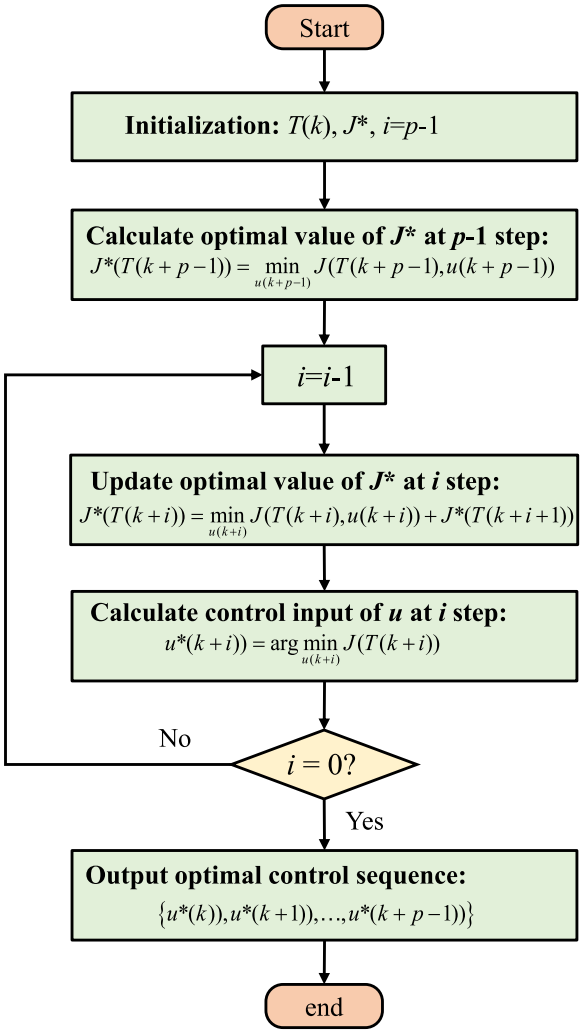

Fig. 5. Flowchart of the rolling optimization process.

In the cooling circuit, the total flow rate and the flow direction are actuated by the pump. The opening of the solenoid valve determines the flow distribution of the two path. The coolant temperature is determined by the chiller, and the power is recorded by the electricity meter. The battery pack conducts the charge/discharge operation through the battery cycler with constant ambient temperature provided by the thermostat. The temperature signals of the battery pack are collected by thermosdetector in real time. The online information of temperature and power is handled by the computer as the feedback to update the control variables.

The liquid cooling loop is composed by the battery pack and heat dissipation components. The coolant temperature is regulated by the chiller through the embedded compressor and heater. As the coolant flowing through the loop, it releases or absorbs the heat in the heat exchanger. The pump maintains the cycle of the cooling loop, and the flow rate is recorded by the flowmeter. It is noteworthy that the control system has a certain hysteresis, and the target control command can not transfer to the BTMS immediately, especially for the coolant temperature.

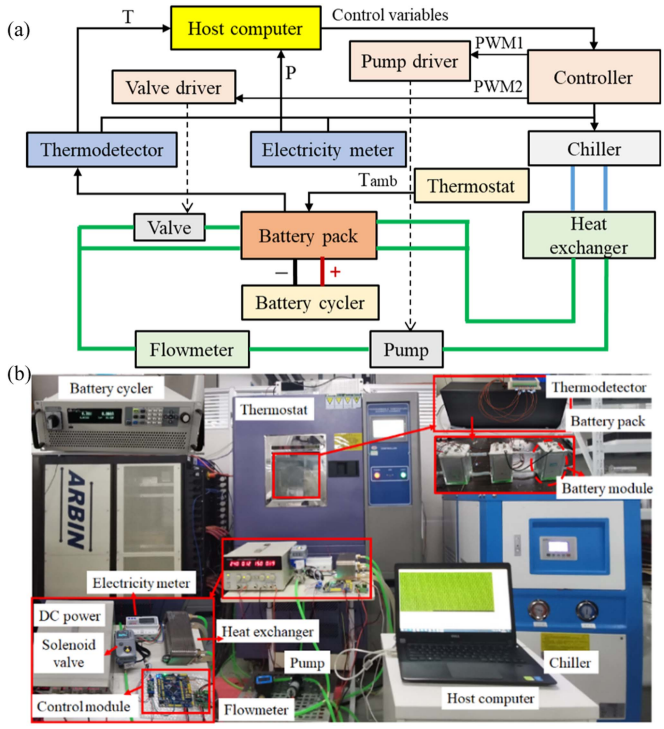

Fig. 6. Test loop of the BTMS control. (a) System diagram. (b) Experimental platform.

Therefore, the changing rate of the control inputs should be considered when formulating the control strategy.

IV. Results and Discussion

To validate the effects of the proposed control strategy, the experiment is carried out under a mix driving cycle with different control schemes. The performance is validated in four aspects: First, the reduced-order multiphysics coupling model is validated. Besides, the prediction effect is analyzed. Then, the thermal performance is analyzed, including the maximum temperature and the temperature uniformity of different layer. Furthermore, the energy consumption and battery health effectiveness are analyzed and compared with other methods.

A. Validation of the Reduced-Order Model

The effectiveness of the model is a prerequisite for predictive control strategy. Therefore, it is essential the validate the proposed model. The model validation is reflected in three submodels. In the electrical model validation, the constant-current discharge test is performed, and the simulated and real voltage is compared as shown in Fig. 7. The results show that the simulated voltage is in good agreement with the measured data with the voltage RMSE being less than 10 mV.

To verify the effectiveness of the FRNM, the calculation results of the flow model are compared with those of the computational fluid dynamics (CFD) model, as displayed in Fig. 8. It is noted that the velocity obtained from the FRNM agrees well with those of the CFD model, with the maximum deviation of

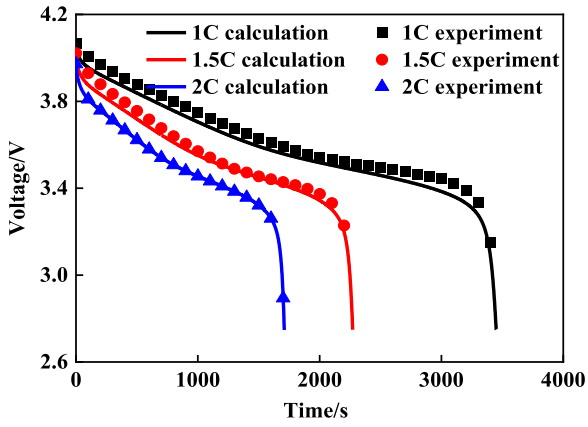

Fig. 7. Validation of the electrical model.

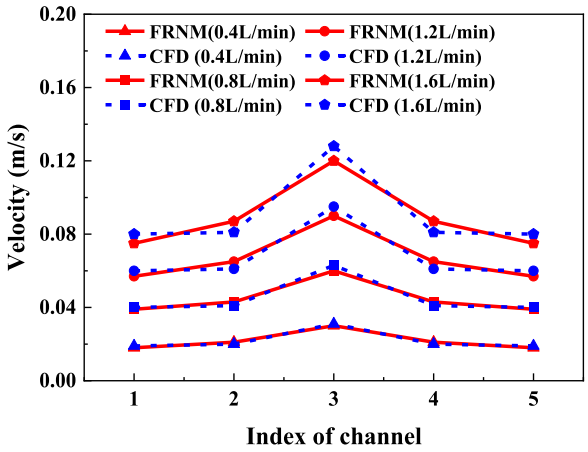

Fig. 8. Validation of the FRNM.

4.1%. The results proved that the simplified flow model meets the accuracy requirements.

In terms of the thermal model, the validation is conducted in three levels, as presented in Fig. 9. In the cell level, the four feature temperatures in the battery cell are used for comparison. The temperatures profile between the experiment and simulation shows a similar tendency, and the maximum error is less than 1.4 °C. In the module level, the temperature performance of different cells in a module is utilized to compare. It can be observed that the proposed model can well depicts the temperature profile among the cells, with the largest deviation being less than 1“°C. In the pack level, the present thermal model trace the temperature dynamic well in different modules with the maximum temperature being less than 2.4“°C.

B. Effects of Different Current Prediction Methods

Fig. 10 shows the predicted current and absolute error in the next 10 s with different forecasting methods, where the traditional grey predicting method and single NARNN are used for comparison. The mean absolute error (MAE) and root mean square error (RMSE) of the three methods are listed in Table III. As shown, the grey predicting methods have the maximum value in these two errors, where some notable deviated exists.

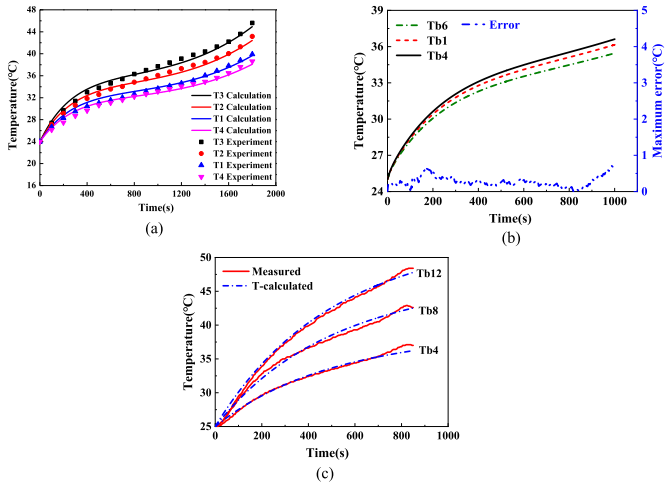

Fig. 9. Validation of the thermal model. (a) Cell level. (b) Module level. (c) Pack level.

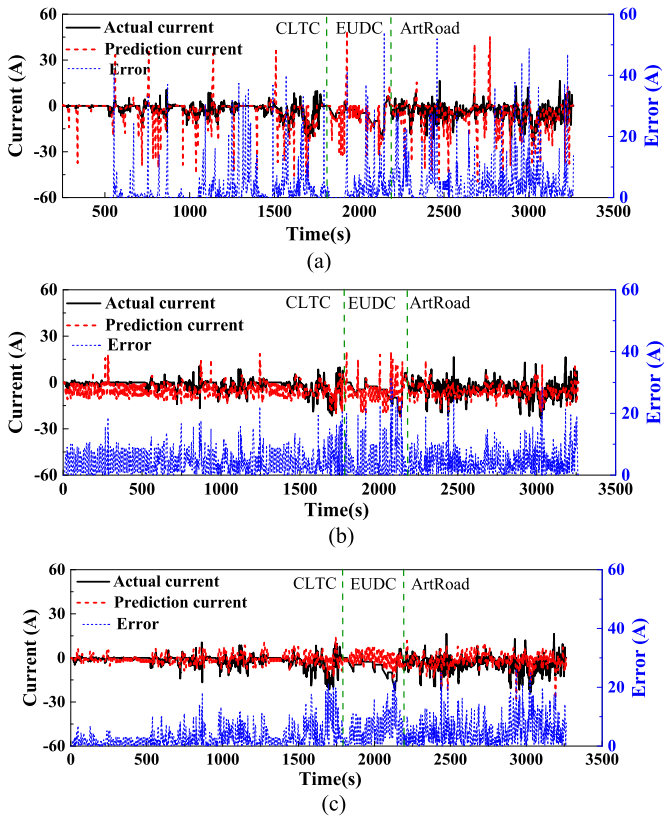

Fig. 10. Predicting results of different predictor in mix driving cycle. (a) Grey prediction. (b) NARNN. (c) BP-NARNN.

TABLE III
PREDICTION ERROR COMPARISON OF THE THREE METHODS

Test driving cycles	Grey prediction (A)		NARNN (A)		BP-NARNN (A)	
	MAE	RSME	MAE	RSME	MAE	RSME
CLTC	8.46	7.63	6.37	5.52	5.02	4.37
EUDC	9.31	8.56	7.18	6.51	5.65	4.83
ArtRoad	7.93	7.37	6.49	5.78	5.17	4.48

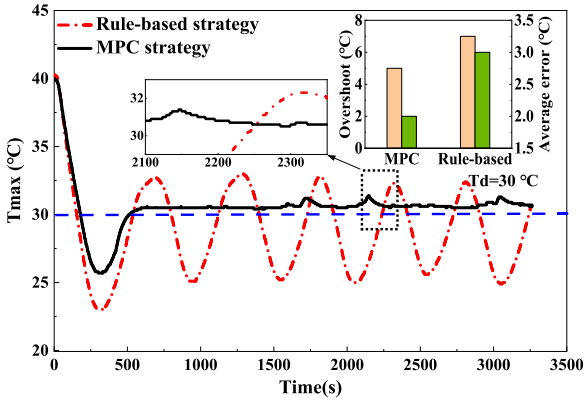

Fig. 11. Comparison of the maximum temperature performance with different control strategies.

When the NARNN is adopted, the stability of prediction results is significantly improved. The forecast accuracy has a further improvement by introducing the operating mode recognition in the BP-NARNN method.

C. Effect and Comparison of the Thermal Control Methods

To evaluate the actual control effectiveness, the thermal performance is analyzed, including the maximum temperature and temperature uniformity at different levels. By comparison, the widely used rule-based control strategy is performed under the same conditions. The rule-based control such as the ON–OFF control and bang-bang control have been widely applied in modern BTMS of EVs. In this study, the bang-bang control principle is adopted as a general rule.

Fig. 11 shows the comparison of the maximum temperature trend with different control strategies. To reflect the control effectiveness of the two control strategies more intuitively, the overshoot and average control error are adopted to indicate the control effect of maximum temperature during the process. It can be seen that $T_{\max}$ is converged to the target temperature with MPC strategy, whereas oscillating near the target with the rule-based strategy. The temperature control effect of the two controllers is acceptable since the optimum battery temperature is within a certain range. Due to the hysteresis of the coolant temperature, the overshoot of temperature is inevitable, and the upper limit of the deviation value is 2“°C, whereas the minimum value of $T_{\max}$ is nearly 25“°C. In comparison, the proposed MPC method has less overshoot with shorter time to steady state (nearly 500 s). Besides, the maximum deviation is less than 1.2“°C after the temperature reaches to the target value. Since the thermal performance can be previewed in the prediction horizon through the reduced-order model, the control inputs can be changed in advance to mitigate the impact of system hysteresis with the MPC method. It can be seen from the entire test process that the maximum overshoot is 7“°C with the rule-based strategy, which is reduced to 4“°C through the MPC strategy. Besides, the average control error of the $T_{\max}$ is reduced by 1/3 when adopted the MPC method.

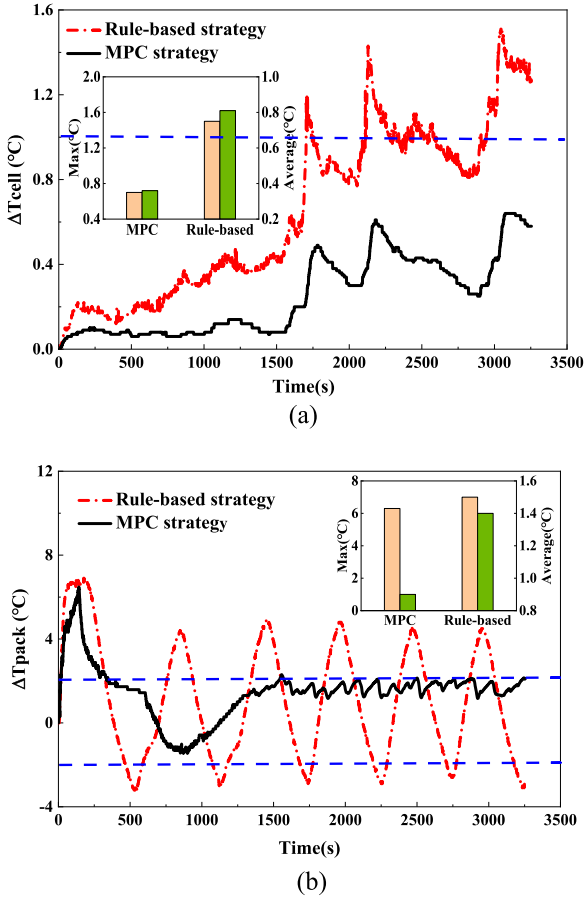

Fig. 12. Temperature uniformity for different control strategies. (a) $\triangle T_{\text{cell}}$. (b) $\triangle T_{\text{pack}}$.

In addition to the maximum temperature, the thermal uniformity of multilayer is also compared. Since the temperature evenness in the module layer is determined by the structure, the temperature uniformity control effect is mainly manifested in cell and pack level, and the responding temperature difference is noted as $\triangle T_{\text{cell}}$ and $\triangle T_{\text{pack}}$.

Fig. 12(a) presents the trend of $\triangle T_{\text{cell}}$ during the mixed cycle. The maximum and average temperature difference are used to reflect the control effect of multilayer temperature distribution. As can be seen that the rule-based control strategy has higher $\triangle T_{\text{cell}}$ than the other controllers, which is up to 1.5“°C in the later stage. The main reason is that the flow distribution is constant that independent of temperature difference information. In comparison, $\triangle T_{\text{cell}}$ can be controlled in 0.8“°C with MPC schemes. Relatively, the MPC controller has better control effect with a smaller variation range. It can also be evidently observed that there are three peaks appeared at the time of 1710 s, 2131 s, and 3043 s, respectively, in the process. It can be concluded that the temperature inhomogeneity in a single cell can be mainly attributed to the current collector, and the larger temperature difference is appeared with higher C-rate. Therefore, the peak of $\triangle T_{\text{cell}}$ is occurred at the moment of continuous high-rate charge/discharge during the cycle. It can be seen observed from the entire test process that both the maximum and average value

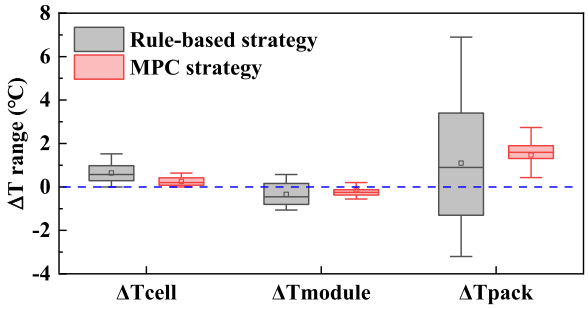

Fig. 13. Multilayer temperature uniformity control effectiveness of different control schemes.

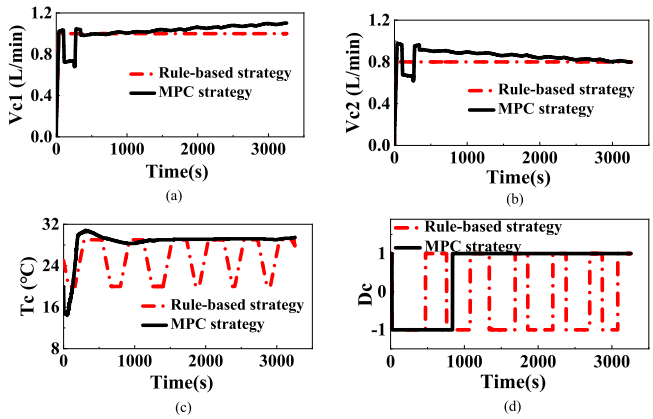

Fig. 14. Comparison of control inputs. (a) V_{c1}. (b) V_{c2}. (c) T_c. (d) D_c.

in MPC strategy is half of them in rule-based strategy, which proves that the proposed method has excellent temperature uniformity control effect in the cell level.

Fig. 12(b) shows the temperature difference of the battery pack, which is calculated by the temperature of batteries in the same position of different module. As can be observed in the results, the rule-based control method has greater fluctuation that generally varies from −3“°C to 4“°C, which is attributed by the synthetic effect of the coolant temperature, flow rate, and flow direction. In terms of the MPC strategy, $\triangle T_{\text{pack}}$ becomes more stable that is basically controlled within 2“°C, and final oscillates around 1.7“°C. In addition, it takes less time to the stable value, and the average value is smallest during the cycle. It is noteworthy that $\triangle T_{\text{pack}}$ surges to the maximum value in the three controllers. The main reason is that the battery pack has the highest temperature of 40“°C at the beginning, so the coolant temperature is set at a lower value to fulfill the control target of $T_{\max}$, which aggravates the temperature difference between the different modules. Since $T_{\max}$ has the highest priority, $\triangle T_{\text{pack}}$ cannot satisfied the optimal range in the meantime. When $T_{\max}$ reaches the expected target after a period of adjustment, $\triangle T_{\text{pack}}$ is able to be controlled in an appropriate range. The statistical results illustrate that stability of temperature difference control is preferable with the MPC strategy.

To give an intuitive contrast of the temperature uniformity effect with different controllers, Fig. 13 displays the statistical chart of the temperature difference that contains the cell, module, and pack level. It can be found that the temperature difference in the cell and module level can be controlled well with different strategies that kept within 1“°C. The MPC method performed better with highest stability and minimum deviation. In the pack level, the obvious discrepancy is exhibited in these two control strategies. On the whole, a relatively ideal fine temperature uniformity is achieved by MPC controller in different level, which is of great significance on thermal consistency of the battery pack.

To further understand the work procedure of the proposed method, Fig. 14 shows the comparison of the control inputs, where the flow rate of the upper and lower cooling channels are noted as V_{c1} and V_{c2}. T_c represents the desired coolant temperature, and D_c is the coolant flow direction, where the value of 1 represents the forward direction, and −1 represents the reverse direction. The comparison of V_{c1} and V_{c2} are shown in Fig. 14(a) and (b), where the rule-based method has the constant flow distribution of 1 L min^{-1} and 0.8 L min^{-1}, respectively. In terms of the MPC controller, the flow distribution varying promptly according to the optimal controller that based on the real-time feedback temperature, where each targets are coordinated to achieve the minimum cost.

A significantly distinction is appeared in T_c as displayed in Fig. 14(c). T_c switches between the regular set temperatures of 20“°C and 29“°C in the rule-based controller. The MPC scheme regulates the coolant temperature according to the $T_{\max}$. T_c decreases sharply at first and then increases gradually as approaching the target temperature, and it finally stabilized within the region of 26“°C to 28“°C. Differ from regulating the inputs after obtaining the feedback temperature, T_c is changed in advance according to the predict tendency. Since the coolant temperature response slowly, the MPC controller improves the response rate and reduce the overshoot of the temperature. The flow direction is converted to the opposite direction when $\triangle T_{\text{pack}}$ exceeds 2“°C, and returning back to the previous direction when$\triangle T_{\text{pack}}$ being less than 1“°C. The rule-based controller changes the flow direction most frequently, whereas the MPC controller changes the flow direction in least frequent, which is conducive to decrease the flow loss of the cooling loop.

D. Energy Consumption and Cycle Life Evaluation

As an important indicator of the BTMS evaluation, the energy consumption comparison is presented in Fig. 15. It can be found that the rule-based control strategy obviously consumes more energy than the MPC scheme, where the energy consumption is up to 60.13 kJ at the end of the operation cycle. In comparison, the MPC method consumes 26.17 kJ in the process. In the early stage, the similar energy consumption rate is appeared with the two strategies. After the time of $t_1 = 456$ s, the value with MPC controller reduced significantly as $T_{\max}$ reaches the steady state. As a result, the MPC strategy saved 56.48% energy cost compared with the rule-based scheme.

The temperature inconsistency has a great impact on lifespan of the battery pack since it aggravates the inconsistent degradation among the batteries [35]. To evaluate the battery health variation caused by the temperature difference, dSOH is

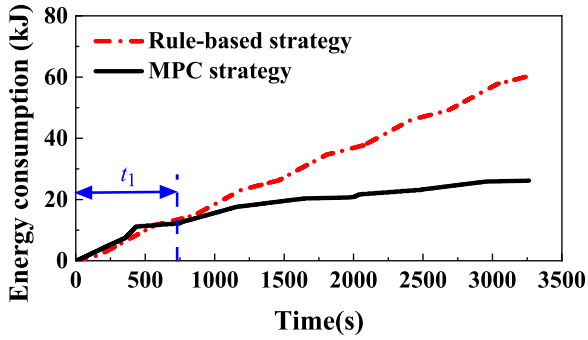

Fig. 15. Energy consumption comparison of different control strategies.

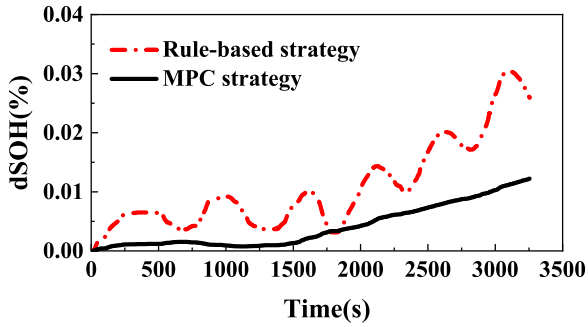

Fig. 16. dSOH comparison under various control strategies.

adopted, which is defined as the SOH difference. An empirical formula is used to calculate the SOH of battery under different temperature according to [36], which is expressed as follows:

$$\begin{aligned} Q_{loss} &= B \cdot \exp\left[(-31700 + 370.3 \cdot C)/RT\right] \cdot A_h^{0.55} \\ SOH(T) &= 1 - Q_{loss}/20\% \\ \text{dSOH} &= SOH(T_{\max}) - SOH(T_{\min}) \end{aligned} \tag{14}$$

where B represents the pre-exponent factor, A_{h} represents the throughput capacity of the battery, and C represents the C-rate. The dSOH comparison with different control schemes is displayed in Fig. 16. It can be found that the dSOH shows a general ascending trend during the mixed-driving cycle, where the value is 0.026% and 0.012% at the end of cycle that responding to the rule-based and MPC strategies, respectively. The MPC controller has the smaller battery health difference due to its better temperature difference control effectiveness, which shows a more obvious advantage in the long-periodic charge/discharge cycles.

To prove the robustness of the proposed control method under various ambient temperatures, the experiments are conducted with the T_{amb} of 10“°C, 20“°C, 40“°C, and 50“°C, respectively. As can be seen in Fig. 17(a) that the maximum temperature can be converged within the target temperature that the maximum fluctuation is less than 1“°C, which proves the effectiveness of the MPC control scheme. The energy consumption is compared in Fig. 17(b). It can be observed from the results that the energy consumption is increased with the temperature difference between the ambient temperature and the target temperature. The

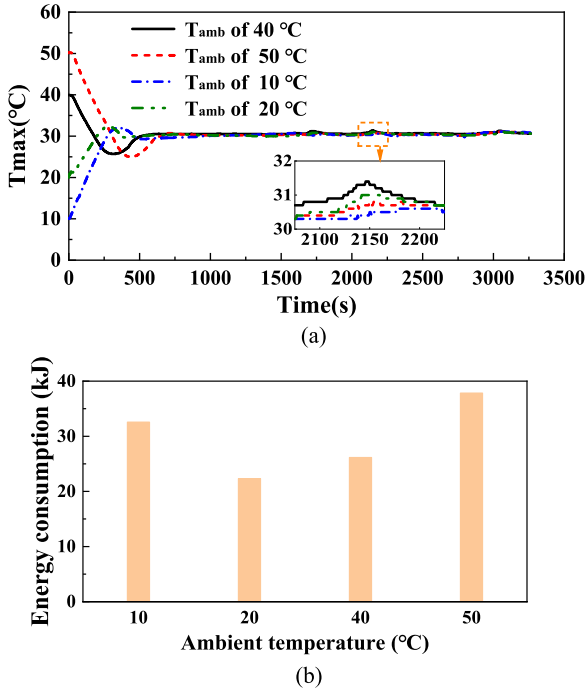

Fig. 17. Control effectiveness at different ambient temperature. (a) Maximum temperature. (b) Energy consumption.

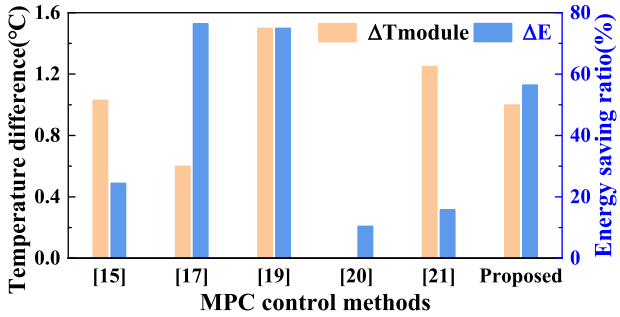

Fig. 18. Performance comparison with different MPC control strategy.

cooling process consume more energy than the heating process under the same temperature difference.

To further evaluate the control effectiveness of the proposed MPC strategy, a comparison is conducted in different BTMSs with the MPC method, as shown in Fig. 18. Since various BTMS has different thermal performance, the comparison is mainly embodied in the improvements of the temperature control and reduction of energy consumption compared with their original control strategy. Most relevant studies are conducted on a battery module rather than a multilayer BTMS, and the maximum temperature is tightly bound to the set value, so ΔT_{module} is utilized to reflect the temperature control effectiveness. In addition, the improvement of energy utilization is always a major concern.

It can be observed that the maximum temperature difference can be controlled within 2“°C, and the MPC-based DCLCS proposed in this work owns the minimum temperature difference of 0.6“°C. In terms of energy consumption rate, the MPC control strategy in [24] has the best effects that approximately 76% of

the energy can be saved by using the MPC method, followed by the proposed MPC-based DCLCS, where 56.48% energy can be reducing in this system. On the whole, good temperature and energy consumption control can be achieved in the proposed method. A dominant superiority of the proposed method is that the fine temperature uniformity can be achieved in different level, from cell to pack, which is benefited from the optimization in control system design and improvement of predictive model.

V. Conclusion

In this article, a fine thermal control has been proposed based on multilayer temperature distribution for a DCLCS. A reduced-order model has been developed for the liquid-based BTMS, where the online estimation of the multilayer temperature distribution could be obtained with low computation burden. Besides, to improve the control effectiveness, a heat generation predictor containing double NN has been integrated in the MPC scheme for the DCLCS. On this basis, the MPC strategy with four control inputs has been applied in the DCLCS experimentally in a mixed driving cycle. As a result, the fine control of the BTMS can be achieved that the temperature difference can be controlled within 0.8“°C, 1“°C, and 2“°C in the cell, module, and pack level, respectively. Compared with the rule-based control strategy, the proposed MPC strategy has faster response with less overshoot in the thermal control. Besides, the energy consumption is reduced by up to 56.48%, and the difference in battery life is the smallest. Additionally, the proposed system owns advantages over other MPC systems in the comprehensive performance.

References

[1] C. Lin, J. Xu, J. Hou, Y. Liang, and X. Mei, “Ensemble method with heterogeneous models for battery state-of-health estimation,” *IEEE Trans. Ind. Inform.*, vol. 19, no. 10, pp. 10160–10169, Oct. 2023.

[2] J. Xu, X. Mei, H. Wang, and J. Wang, “A hybrid self-heating method for batteries used at low temperature,” *IEEE Trans. Ind. Inform.*, vol. 17, no. 7, pp. 4714–4723, Jul. 2021, doi: 10.1109/TII.2020.3020302.

[3] L. Ianniciello, P. H. Biwolé, and P. Achard, “Electric vehicles batteries thermal management systems employing phase change materials,” *J. Power Sources*, vol. 378, pp. 383–403, 2018.

[4] Z. Guo, J. Xu, Z. Xu, M. Mubashir, H. Wang, and X. Mei, “A three-heat-source electro-thermal coupled model for fast estimation of the temperature distribution of a lithium-ion battery cell,” *IEEE Trans. Transp. Electrific.*, vol. 8, no. 1, pp. 288–297, Mar. 2022.

[5] Z. Song, N. Yang, X. Lin, F. Pinto Delgado, H. Hofmann, and J. Sun, “Progression of cell-to-cell variation within battery modules under different cooling structures,” *Appl. Energy*, vol. 312, 2022, Art. no. 118836.

[6] J. Xu, X. Mei, X. Wang, Y. Fu, Y. Zhao, and J. Wang, “A relative state of health estimation method based on wavelet analysis for lithium-ion battery cells,” *IEEE Trans. Ind. Electron.*, vol. 68, no. 8, pp. 6973–6981, Aug. 2021.

[7] J. Xu, Z. Guo, Z. Xu, X. Zhou, and X. Mei, “A systematic review and comparison of liquid-based cooling system for lithium-ion batteries,” *eTransportation*, vol. 17, 2023, Art. no. 100242.

[8] C. Zhu, F. Lu, H. Zhang, J. Sun, and C. C. Mi, “A real-time battery thermal management strategy for connected and automated hybrid electric vehicles (CAHEVs) based on iterative dynamic programming,” *IEEE Trans. Veh. Technol.*, vol. 67, no. 9, pp. 8077–8084, Sep. 2018.

[9] M. R. Amini, H. Wang, X. Gong, D. Liao-McPherson, I. Kolmanovsky, and J. Sun, “Cabin and battery thermal management of connected and automated HEVs for improved energy efficiency using hierarchical model predictive control,” *IEEE Trans. Control Syst. Technol.*, vol. 28, no. 5, pp. 1711–1726, Sep. 2020.

[10] Z. Guo, J. Xu, Z. Xu, M. Mubashir, H. Wang, and X. Mei, “A lightweight multichannel direct contact liquid-cooling system and its optimization for lithium-ion batteries,” *IEEE Trans. Transp. Electrific.*, vol. 8, no. 2, pp. 2334–2345, Jun. 2022.

[11] M. A. Jeffers, L. Chaney, and J. P. Rugh, “Climate control load reduction strategies for electric drive vehicles in warm weather,” in *Proc. SAE World Congr. Exhib.*, 2015, pp. 1–11.

[12] Y. Zeng, D. Chalise, S. D. Lubner, S. Kaur, and R. S. Prasher, “A review of thermal physics and management inside lithium-ion batteries for high energy density and fast charging,” *Energy Storage Mater.*, vol. 41, pp. 264–288, 2021.

[13] Y. Fu, J. Xu, M. Shi, and X. Mei, “A fast impedance calculation based battery state-of-health estimation method,” *IEEE Trans. Ind. Electron.*, vol. 69, no. 7, pp. 7019–7028, Jul. 2022.

[14] C. Wu, J. Zhao, C. Liu, and Z. Rao, “Performance and prediction of baffled cold plate based battery thermal management system,” *Appl. Thermal Eng.*, vol. 219, 2023, Art. no. 119466.

[15] K. Li, H. Chen, J. Zhao, L. Eriksson, and J. Gao, “An advanced control strategy for engine thermal management systems with large pure time delay,” *Appl. Thermal Eng.*, vol. 224, 2023, Art. no. 120084.

[16] T. H. Pham, J. T. Kessels, P. Bosch, R. Huisman, and R. Nevels, “On-line energy and battery thermal management for hybrid electric heavy-duty truck,” in *Proc. Amer. Control Conf.*, 2013, pp. 710–715.

[17] J. Cen and F. Jiang, “Li-ion power battery temperature control by a battery thermal management and vehicle cabin air conditioning integrated system,” *Energy Sustain. Develop.*, vol. 57, pp. 141–148, 2020.

[18] F. Nur, M. Hawlader, R. Afroz, and A. Rahman, “Fuzzy controlled evaporative battery thermal management system for EV/HEV,” *Int. J. Electric Hybrid Veh.*, vol. 7, pp. 22–39, 2015.

[19] H. Wang and L. Ma, “Thermal management of a large prismatic battery pack based on reciprocating flow and active control,” *Int. J. Heat Mass Transfer*, vol. 115, pp. 296–303, 2017.

[20] W. Lee, H. Jeoung, D. Park, and N. Kim, “An adaptive concept of PMP-based control for saving operating costs of extended-range electric vehicles,” *IEEE Trans. Veh. Technol.*, vol. 68, no. 12, pp. 11505–11512, Dec. 2019.

[21] Y. Masoudi, A. Mozaffari, and N. L. Azad, “Battery thermal management of electric vehicles: An optimal control approach,” in *Proc. ASME Dyn. Syst. Control Conf.*, 2015.

[22] Y. Xie, C. Wang, X. Hu, X. Lin, Y. Zhang, and W. Li, “An MPC-based control strategy for electric vehicle battery cooling considering energy saving and battery lifespan,” *IEEE Trans. Veh. Technol.*, vol. 69, no. 12, pp. 14657–14673, Dec. 2020.

[23] W. Zhuang, Z. Liu, H. Su, and G. Chen, “An intelligent thermal management system for optimized lithium-ion battery pack,” *Appl. Thermal Eng.*, vol. 189, 2021, Art. no. 116767.

[24] S. Park and C. Ahn, “Computationally efficient stochastic model predictive controller for battery thermal management of electric vehicle,” *IEEE Trans. Veh. Technol.*, vol. 69, no. 8, pp. 8407–8419, Aug. 2020.

[25] Z. Shuofeng, M. R. Amini, J. Sun, and C. Mi, “A two-layer real-time optimization control strategy for integrated battery thermal management and HVAC system in connected and automated HEVs,” *IEEE Trans. Veh. Technol.*, vol. 70, no. 7, pp. 6567–6576, Jul. 2021.

[26] S. Zhao and C. C. Mi, “A two-stage real-time optimized EV battery cooling control based on hierarchical and iterative dynamic programming and MPC,” *IEEE Trans. Intell. Transp. Syst.*, vol. 23, no. 8, pp. 11677–11687, Aug. 2021.

[27] M. R. Amini, I. Kolmanovsky, and J. Sun, “Hierarchical MPC for robust eco-cooling of connected and automated vehicles and its application to electric vehicle battery thermal management,” *IEEE Trans. Control Syst. Technol.*, vol. 29, no. 1, pp. 316–328, Jan. 2021.

[28] Y. Liu and J. Zhang, “Design a J-type air-based battery thermal management system through surrogate-based optimization,” *Appl. Energy*, vol. 252, 2019, Art. no. 113426.

[29] Y. Liu and J. Zhang, “Self-adapting J-type air-based battery thermal management system via model predictive control,” *Appl. Energy*, vol. 263, 2020, Art. no. 114640.

[30] K. Murashko, J. Pyrhonen, and L. Laurila, “Three-dimensional thermal model of a lithium ion battery for hybrid mobile working machines: Determination of the model parameters in a pouch cell,” *IEEE Trans. Energy Convers.*, vol. 28, no. 2, pp. 335–343, Jun. 2013.

[31] M. Chen et al., “A multilayer electro-thermal model of pouch battery during normal discharge and internal short circuit process,” *Appl. Thermal Eng.*, vol. 120, pp. 506–516, 2017.

[32] J. Zhang, X. Wu, K. Chen, D. Zhou, and M. Song, "Experimental and numerical studies on an efficient transient heat transfer model for air-cooled battery thermal management systems," *J. Power Sources*, vol. 490, 2021, Art. no. 229539.
[33] Y. Li, J. Zhang, C. Ren, and X. Lu, "Prediction of vehicle energy consumption on a planned route based on speed feature parameters forecasting," *IET Intell. Transport Syst.*, vol. 14, no. 3, pp. 511–522, 2020.
[34] C. Lin, J. Xu, and X. Mei, "Improving state-of-health estimation for lithium-ion batteries via unlabeled charging data," *Energy Storage Mater.*, vol. 54, pp. 85–97, 2023.
[35] Q. Xia et al., "Multiphysical modeling for life analysis of lithium-ion battery pack in electric vehicles," *Renewable Sustain. Energy Rev.*, vol. 131, 2020, Art. no. 109993.
[36] J. Wang et al., "Cycle-life model for graphite-LiFePO4 cells," *J. Power Sources*, vol. 196, no. 8, pp. 3942–3948, 2011.

Zhechen Guo received the B.S. degree in energy and power engineering from Chang'an University, Xi'an, China, in 2016, and the M.S. degree in energy and power engineering in 2019 from Xi'an Jiaotong University, Xi'an, China, where he is currently working toward the Ph.D. degree in mechanical engineering with the School of Mechanical Engineering.

His research interests include energy management for lithium-ion battery, especially the research of battery thermal management.

Jun Xu (Senior Member, IEEE) received the B.S. and Ph.D. degrees in mechanical engineering from Xi'an Jiaotong University, Xi'an, China, in 2009 and 2013, respectively.

From 2011 to 2013, he was a Joint Ph.D. Student with the U.S. Department of Energy GATE Center for Electric Drive Transportation, College of Electrical and Computer Science, University of Michigan, Dearborn, MI, USA. He is currently a Professor with the School of Mechanical Engineering, Xi'an Jiaotong University. He has conducted extensive research and authored more than 90 peer-reviewed papers. He holds more than 20 patents. His research interests include design, modeling, control of battery systems, electric vehicles, renewable energy systems, and robots.

Dr. Xu was the recipient of the Innovation Award of the China Industry-University-Research Cooperation Innovation Award, the First Prize of the Shaanxi Province University Science and Technology Award, the Second Prize of the Shaanxi Province Teaching Achievement Award, and the Special Award of the Xi'an Jiaotong University Teaching Achievement Award. He was the Conference Chair, the Organizing Committee Co-Chair, and the Conference Academic Committee Member for several international conferences.

Xingzao Wang received the B.S. degree in vehicle engineering major from Harbin Institute of Technology, Weihai, China, in 2021. He is currently working toward the Ph.D. degree in mechanical engineering with the School of Mechanical Engineering, Xi'an Jiaotong University, Xi'an, China.

His research focuses on the area of battery thermal management systems.

Jinwen Shi received the B.S. and Ph.D. degrees in power engineering and engineering thermophysics from Xi'an Jiaotong University, Xi'an, China, in 2005 and 2012, respectively.

He is currently a Professor with the State Key Laboratory of Multiphase Flow in Power Engineering, School of Energy and Power Engineering, Xi'an Jiaotong University. His research interests include solar-to-hydrogen, carbon capture and utilization, and atmospheric water gathering.

Enhu Li received the B.S. degree in automatic control major from Xi'an Technological University, Xi'an, China, in 2003.

He is currently the Executive Vice President of Gresgying Digital Energy Technology Company, Ltd., Xianyang, China. His research interests include charging of electrical vehicle, energy storage, and microgrids system.

Xuesong Mei received the Ph.D. degree in mechanical engineering from Xi'an Jiaotong University, Xi'an, China, in 1991.

He is currently a Full Professor with the School of Mechanical Engineering, and the Director of the Shaanxi Key Laboratory of Intelligent Robots, Xi'an Jiaotong University. His research interests include intelligent manufacturing, robotics, and precision laser processing.